Composite Structures 322 (2023) 117338

Contents lists available at ScienceDirect

Composite Structures

journal homepage: www.elsevier.com/locate/compstruct

Tension-after-impact (TAI) performance and 3D damage visualization of carbon-fiber epoxy composites with adhesively bonded patch repairs

Florian Roeper (Röper)[a], Silvano Sommacal[b], Paul Compston[c], Jürgen Tauchner[d], Markus Wolfahrt[e,*], Gerald Pinter[f]

[a] Polymer Competence Center Leoben GmbH, 8700 Leoben, Austria
[b] ARC Training Centre for Automated Manufacture of Advanced Composites, Research School of Electrical, Energy and Materials Engineering, Australian National University, Canberra, ACT 2600, Australia
[c] ARC Training Centre for Automated Manufacture of Advanced Composites, Research School of Electrical, Energy and Materials Engineering, Australian National University, Canberra, ACT 2600, Australia
[d] FACC Operations GmbH, 4973 St. Martin im Innkreis, Austria
[e] Polymer Competence Center Leoben GmbH, 8700 Leoben, Austria
[f] Chair of Material Science and Testing of Polymers, Montanuniversität Leoben, 8700 Leoben, Austria

A R T I C L E I N F O

Keywords:
B Impact behavior
D CT analysis
D Mechanical testing
E Joints/joining

A B S T R A C T

Bonded repairs are advantageous for the aircraft industry when applying repairs to composite parts. However, their post-impact behavior under mechanical loads has to be addressed. Within this study, CFRP specimens repaired via a soft-patch repair approach as well as pristine (i.e. virgin) laminates without repairs, were impacted (energy: 5 J to 30 J). Subsequently, tensile tests were performed in order to investigate their post-impact mechanical properties. For selected impact energy levels, a detailed analysis on the extent of damage was conducted by micro-CT imaging. From these investigations, the interrelation of the impact energy, the mechanical properties obtained from the post-impact tensile tests as well as of the extent (quantitative and qualitative) and nature of damage could be studied and visualized in 2D and 3D images. Furthermore, a high-resolution image acquired on an undamaged repair-specimen was segmented, from which the individual bond constituents could be identified and visualized in 3D representations.

1. Introduction

Polymer matrix composites, especially carbon fiber reinforced polymers (CFRP) found acceptance in the civil as well as the military aircraft sector in all types of structures (primary, secondary as well as tertiary/cabin interior) [1–5]. One of the latest aircraft manufactured by Airbus, the A350, consists of roughly 50 % composites by weight [6,7]. Especially the use in primary, load bearing structures, which lead to catastrophic events in case of failure [8], leads to the demand for repair strategies suitable for CFRP [9,10]. In terms of e. g. load transfer as well as weight savings and the absence of drilled holes to the composite structure, when compared to mechanically fastened repairs, bonded patch repairs offer several advantages for CFRP [10,11]. In recent years the scope of studies that were conducted on bonded repairs for composite structures was extended from the investigation of static strength and the related influencing factors (e.g. joint geometry, surface preparation and environmental conditions) [9,10,12–15] towards damage tolerance behavior. The investigation of damage tolerance behavior is of importance because CFRP are in general susceptible to impact events causing internal damage (e.g. delamination or matrix cracks) resulting in e.g. a deterioration of strength and stiffness [16–19]. Especially low velocity impact, typically causing extended internal but minor external damage, is of concern for the aircraft industry because there is the risk of it passing undetected [18–22]. The characterization and understanding of damage mechanisms resulting from impact events is highly important for both, the design as well as the modelling process of composite structures [18], consequently it is also important to understand these for bonded composite repairs, additionally to the assessment of the damage tolerance of repaired laminates [23,24]. In recent years, X-ray micro-computed tomography (micro-CT) has proven to be an ideal, non-destructive characterization technique that provides high-resolution,

* Corresponding author at: Polymer Competence Center Leoben GmbH, 8700 Leoben, Austria.
E-mail addresses: florian.roeper@pccl.at (F. Roeper), silvano.sommacal@anu.edu.au (S. Sommacal), paul.compston@anu.edu.au (P. Compston), J.Tauchner@facc.com (J. Tauchner), markus.wolfahrt@pccl.at (M. Wolfahrt), gerald.pinter@unileoben.ac.at (G. Pinter).

https://doi.org/10.1016/j.compstruct.2023.117338
Received 22 March 2022; Received in revised form 16 May 2023; Accepted 6 July 2023
Available online 7 July 2023

Abbreviations

CFRP	Carbon Fiber Reinforced Polymers
CAI	Compression After Impact
DIC	Digital Image Correlation
micro-CT	X-ray micro-Computed Tomography
ROI	Regions Of Interest
TAI	Tensile After Impact

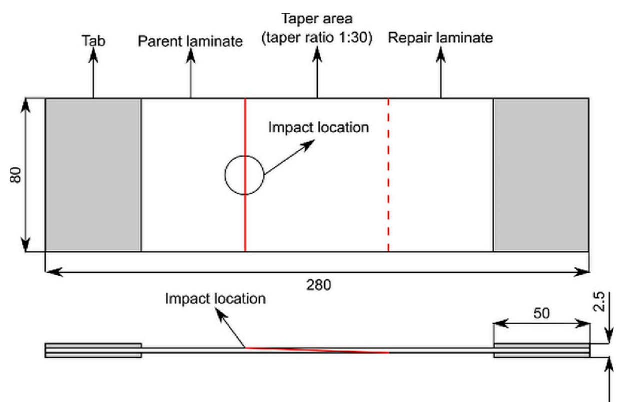

a

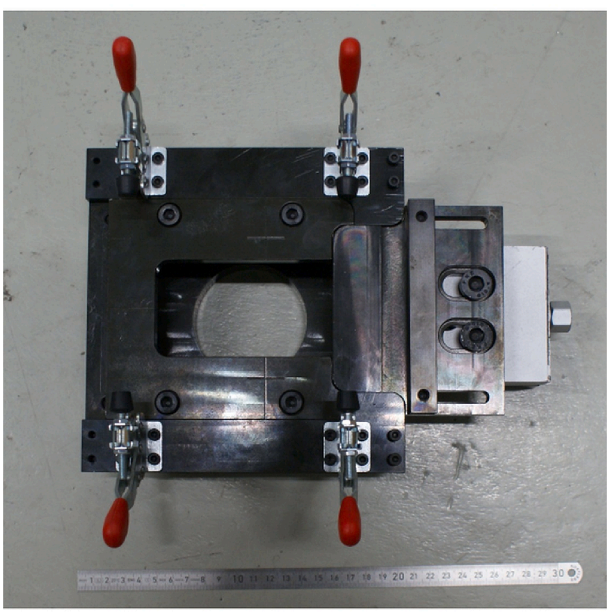

b

Fig. 1. A) Repaired TAI specimen with impact location indicated, all dimensions in mm. b) Impact fixture with levers for specimen fixation during impact and cut-out area.

high-quality 3D images of internal damage and can therefore be utilized for the assessment of damage mechanisms and propagation occurring in CFRP [18–21].

Comprehensive literature reviews are available dealing with the post-impact behavior of composites under tension and compression loading (see e.g.: [25–31]). A few studies were conducted on the compression after impact (CAI) strength of thin laminates with a specifically designed compression devices to avoid buckling [32,33]. Experimental tests on the compression after impact behavior of scarf repair composite have been performed for 2D [4,34] as well for 3D [16,24,35] patch repairs.

However, only a few studies concentrate on the tensile after impact (TAI) strength of repairs [34,36–38]. Publications regarding CT inspections aiming at the investigation of damage resulting from impact events were published by e. g. by Bull et al. [39,40], Senck et al. [41] and Leonard et al. [18]. The present study combines TAI tests on adhesively bonded, scarfed repairs of CFRP with micro-CT inspections. Due to the fact that the specimens' thickness was significantly lower than described in the relevant ASTM standard [42] covering compression after impact tests, the specimens were more prone to buckling under compression loading. Several anti-buckling devices described in literature were used within simulations of the compression tests including the investigated laminate geometry. Ultimately, tension after impact tests were conducted because none of these anti-buckling devices could prevent buckling prior to failure.

Impact tests with selected energy levels were performed on repaired as well as pristine (virgin) CFRP specimens. Subsequent to the impact tests, TAI tests were carried out in order to assess the post-impact mechanical properties of both specimen types in comparison to non-damaged ones. The micro-CT inspections were performed with the intention to (i) visualize and characterize the post-impact damage patterns in 2D and 3D, to (ii) visualize and quantify the projected damaged areas and to (iii) perform a detailed 3D micron-scale characterization of the material microstructure on a small volume extracted from a repaired, undamaged specimen.

This arrangement of experiments is, to the authors' knowledge, quite novel in literature. It offers a unique perspective to the mechanical post-impact damage behavior of repaired specimens in comparison to pristine laminates in combination with qualitative and quantitative insights gained by micro-CT with respect to damage patterns as well as the repaired laminates' microstructure.

1.1. *Materials and specimen production*

Only a brief summary of the specimen production procedure will be given at this point, because the respective procedure was already described in a previous publication [15]. It has to be noted, that the width of the specimens was increased in comparison to the cited paper and to the according standard, which is intended for tensile testing of tapered joints [43]. Also, the taper ratio of the repaired specimens was changed. In the previous paper, a taper ratio of 1:9 resulting in a taper angle of 6.3° was used [15]. In this publication, specimens were produced with a taper ratio of 1:30, resulting in a less steep taper angle of 1.9°.

Initially, laminate plates were manufactured from an epoxy-based, woven carbon fiber reinforced Cytec Cycom 977-2 prepreg material (Tempe, AZ, US) [44], which was cured in an autoclave at 180 °C for 2 h at 6.6 bar. The respective stacking sequence, $[(\pm45)/(0/90)/(\pm45)/(0/90)]_S$, resulted in a quasi-isotropic laminate. From these plates, two types of specimens were produced for the impact and the subsequent TAI tests: (i) pristine (virgin) specimens without repair (used as a basis for comparison or a "reference", respectively) as well as (ii) specimens simulating bonded repairs (repair-specimens).

For (i), tapered end tabs (glass fiber reinforced epoxy laminate) were bonded by 3 M Scotch-Weld AF163-2L (Saint Paul, MN, US) [45], an epoxy-based film adhesive, to laminate plates that were cut from the original, cured laminates. Curing of the film adhesive was achieved in a plate press (P300 E+, Dr. Collin, Ebersberg, DE) according to the manufacturer's specifications at 120 °C for 1 h. Subsequently, individual specimens with dimensions according to the repaired ones (see Fig. 1) were cut from these plates by a diamond coated blade mounted on a water-cooled circular saw (Diadisc 5200, Mutronic Präzisionsgerätebau, Rieden, DE).

For (ii), a repair approach by a soft patch, composed of the same type

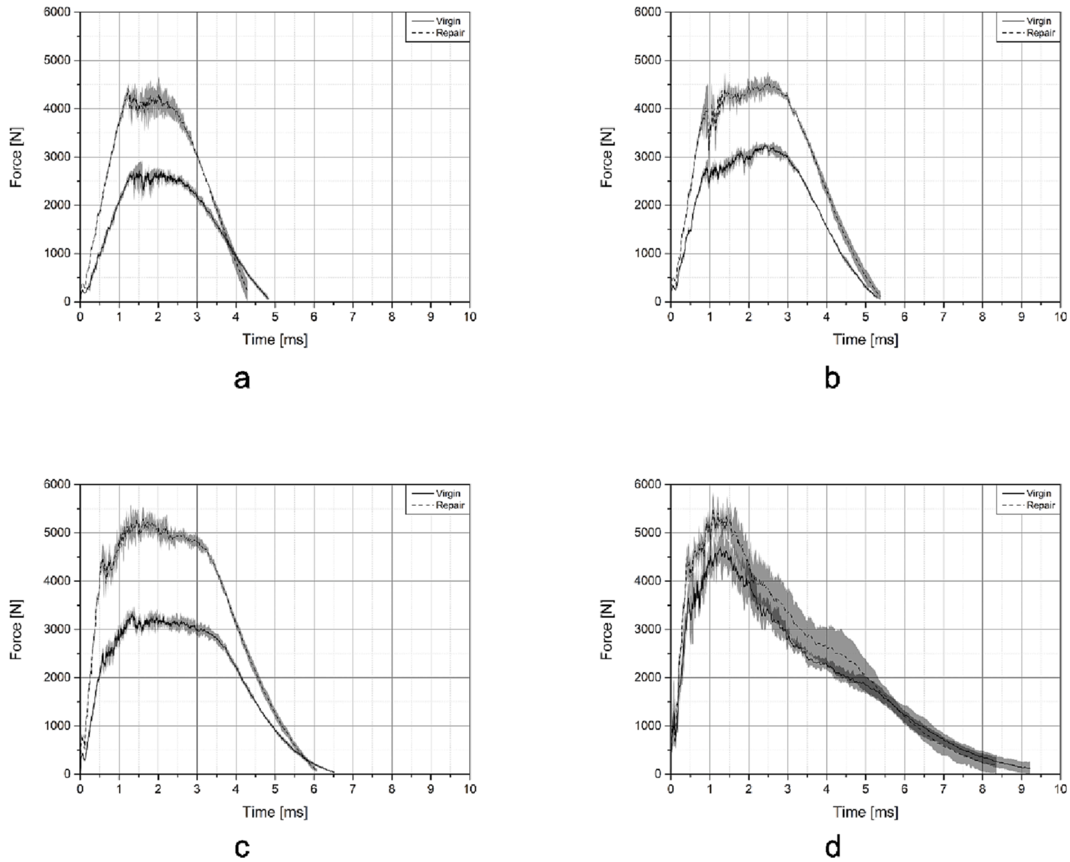

Fig. 2. Plots of force vs. time (as mean curve with standard deviation as shaded area surrounding the respective curve) for impact on virgin as well as repair specimens with (a) 5 J, (b) 10 J, (c) 20 J, (d) 30 J.

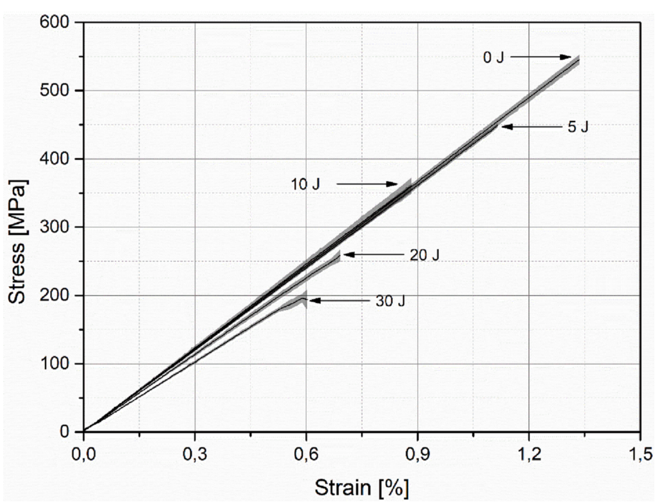

Fig. 3. Stress vs. strain curves of virgin specimens in undamaged (non-impacted, i.e. 0 J) as well as damaged state (impact with 5 J, 10 J, 20 J, 30 J) as mean curves with standard deviation as shaded area surrounding the respective curves.

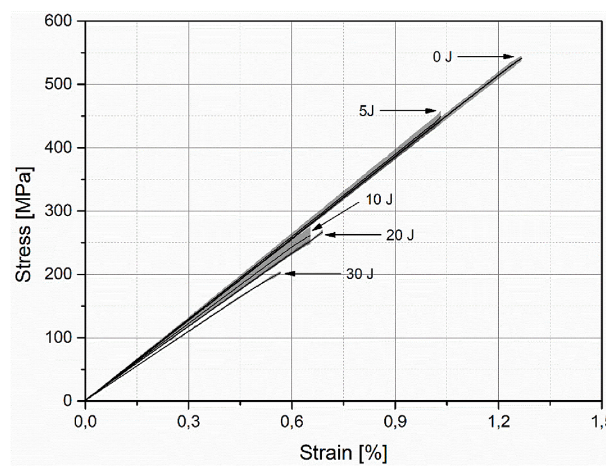

Fig. 4. Stress vs. strain curves of repaired specimens in undamaged (non-impacted, i.e. 0 J) as well as damaged state (impact with 5 J, 10 J, 20 J, 30 J) as mean curves with standard deviation as shaded area surrounding the respective curves.

of prepreg material as used for manufacturing of the original laminate, was chosen. In contrast to a repair performed with a pre-cured repair patch (secondary bonding of pre-cured patch via adhesive), the patch is laid up ply by ply and subsequently cured (co-curing of adhesive and repair plies) [7,46,47]. Prior to the repair patch placement, the original laminate had to be tapered by milling followed by hand-sanding according to the taper ratio of 1:30. The patch was placed ply by ply on the tapered area, subsequent to one plie of an epoxy-based Cytec FM300K 0.05 film adhesive (Tempe, AZ, US) [48] including a knit polyester carrier, thereby restoring the original stacking sequence of the laminate. Vacuum debulking was performed after the lay-up of two plies was completed for 10 min each. Curing of the repair patch was performed similar to the original laminate in a co-bonding procedure. Subsequent to the curing process, tabs were attached to the repaired plates followed by cutting of the individual specimens, as described above for (i).

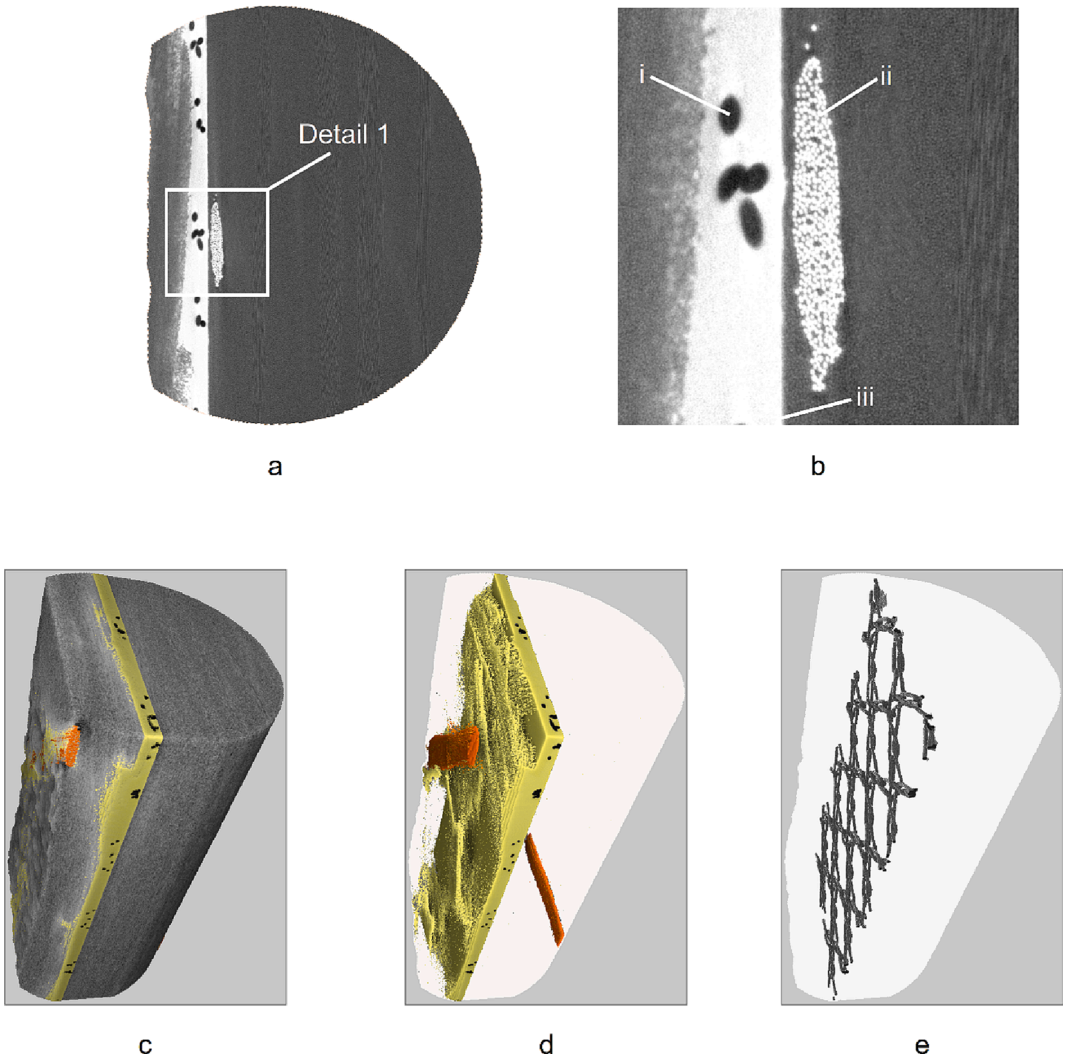

Fig. 5. (a) 2D tomogram images from the high resolution ROI scan (cylindrical ROI image with 3.7 mm diameter resulting in ~1.5 µm voxel size) acquired on the undamaged repaired sample (ROI-0 J-repair) with the purpose of investigating the sample's constituents, (b) magnification of Detail 1 where (i) the knit carrier incorporated in (iii) the film adhesive and (ii) the tracer yarns can be identified within the virgin/repair laminate, (c)–(e) 3D visualizations of segmented images obtained for a subset of the ROI-0 J-repair tomogram image, where (c) all constituents, (d) the adhesive, the knit carrier incorporated in the adhesive as well as the tracer yarns and (e) the knit carrier without the surrounding adhesive are shown.

1.2. *Experimental procedures*

1.2.1. *Impact tests*

Impact tests were performed using ASTM D 7136 – 15 as guidance [42]. However, in order to adapt to the changes in specimen geometry and nature, a specimen clamping device had to be constructed. This device mainly consisted of 3 major components: (i) Base-plate with adaptor for mounting to the Instron CEAST 9350 drop weight impact tower (ITW Test and Instrument Italia S.r.L. – INSTRON CEAST Division, Pianezza, IT) (ii) Specimen support with cut-out (unsupported area where the impact event takes place) including an adjustable section in order to adapt for tab thickness, as impacts were performed with end tabs already in place. In accordance with the cited standard, 4 clamping devices were holding the specimens in place during the impact event. It is important to note that the geometry of the specimen support as well as of the cut-out were scaled according to the lower width of the specimens used in this study compared to the width specified in the ASTM 7136 standard [42]. The impact location was centered within the cut-out. However, specimens were aligned eccentrically within the clamping device in order to ensure that the impact could be performed at the center of the repaired specimens' scarf tip (see Fig. 1 (a) and (b) for details on the specimens as well as of the impact device), which was found to be critical in other studies [37]. The virgin specimens were impacted at the same position (i.e. the impact location had the same distance from the clamping devices used within the subsequent tension tests for both, the virgin as well as the repaired specimens). Another important fact is, that the thickness of the specimens used in this study is significantly lower (2.5 mm) than proposed by the according ASTM standard [42]. At least 4 specimens have been used for the impact tests. One specimen impacted with 5 J as well as one specimen impacted with 20 J was used for the micro-CT investigations. Hence, a discrepancy exists between the number of specimens used for impact tests and the number of specimens used in the quasi-static tensile tests.

Impact tests were performed at fixed energy levels (E) of 5 J, 10 J, 20 J and 30 J, respectively. This spectrum of impact energies resembles in service conditions encountered by thin laminates [18]. The according drop height (h) was calculated by rearranging the formula for the calculation of potential energy ($E = m*g*h$) accordingly from the desired energy level (E) as well as from the impactor mass (m) of 2.63 kg and the gravitational acceleration (g) (9.81 m/s^2). The nominal impact velocities were 1.95 m/s (5 J), 2.76 m/s (10 J), 3.90 m/s (20 J) and 4.78 m/s (30 J). The striker itself had a hemispherical striker tip with a diameter of 20

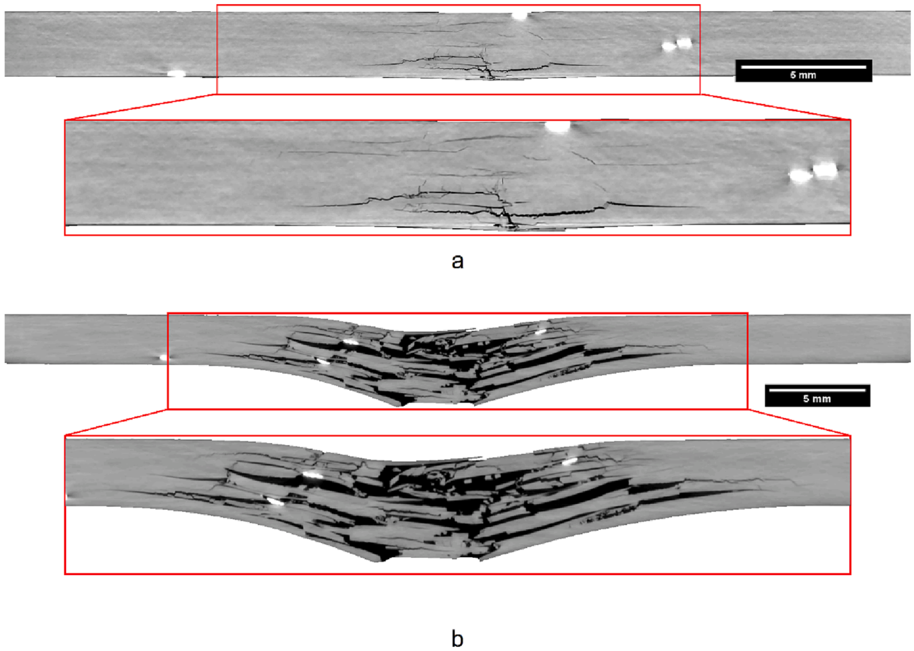

Fig. 6. 2D tomogram images of virgin samples impacted with (a) 5 J (ROI-5 J-virgin, scanning resolution of 14 µm) and (b) 20 J (ROI-20 J-virgin, scanning resolution of 19 µm). Please note that the scalebars have been inserted manually using ImageJ [57].

mm and was instrumented with a piezoelectric load cell (36 kN load range). In order to prevent the striker from re-impacting the specimens subsequent to the initial impact, the drop tower's anti-rebound system was activated.

1.2.2. Quasistatic tensile tests

Comparable to the description of specimen manufacturing, only a brief summary of the procedure for quasi-static tensile testing will be given, as a detailed description can be found in [15]. Quasi-static tensile tests were performed in accordance with DIN prEN 6066 [43] (except for the changes in specimen geometry and the presence of impact damage, respectively) on a 250 kN universal tensile/compression test machine (Z250, Zwick, Ulm, DE). Specimens were loaded via wedge-screw grips (250 kN maximum load) at a test speed of 2 mm/min with an initial gage section of 160 mm. Loads were recorded by a 250 kN load cell. At least 3 specimens have been used for the quasi-static tensile tests.

Strain measurements were performed using a Mercury RT (Sobriety s.r.o., Kuřim, CZ) full field 3D digital image correlation (DIC) system equipped with two 29 megapixel cameras (Prosilica GT 6600, Allied Vision, Stadtroda, DE) in combination with Nikkor 105 mm f/1.8 lenses (Nikon, Tokya, JP). For this purpose, a speckle pattern was sprayed to the specimen surfaces that have been facing the striker during the impact tests. In order to achieve strong contrast, the pattern consisted of graphite spray (Graphit 33, CRC Industries Europe, Zele, BE) on a white spray-primer (Nord Test Entwickler U89, Helling, Heidgraben, DE).

1.2.3. Computed tomography

All CT images utilized for this work have been acquired at the Australian National University's (ANU) CT laboratory on a micro-CT instrument equipped with a flat panel detector (3040 × 3040 pixel) and a 60 kV micro-focus X-ray source. Inside the micro-CT chamber, the specimens were placed on a motor-controlled rotating stage. Radioscope projections were taken after each interval of rotation. Subsequently, a 3D reconstruction from the grayscale projections was performed using proprietary ANU Helical Reconstruction software [49].

To thoroughly inspect and characterize the damaged area in 3D, a multi-scale imaging approach was followed. As a first step, overview images of six specimens were acquired (virgin and repaired specimens both in undamaged state, i.e. 0 J, as well as after 5 J and 20 J impact, respectively) at a scanning resolution, i.e. voxel size, of 32 µm. These images were used to investigate the material's main structural features and to map the damage extent in order to identify smaller regions of interest (ROIs) in each of the four damaged samples to be further investigated at higher resolution. In the next step, the selected ROI volumes, which were subsequently imaged at a scanning resolution of 14 µm (specimen designation: ROI-5 J-virgin/repair) and 19 µm (ROI-20 J-virgin/repair), respectively, were extracted from the damaged samples using a diamond saw (LECO VC50 Precision Diamond Saw).

In parallel, one specimen with a cross section of ~3.2 × 4.1 mm and a length of 48 mm was cut from the undamaged repaired sample, using the same diamond saw. On that specimen, a cylindrical (~3.7 mm diameter) ROI image was acquired by micro-CT at a higher scanning resolution of 1.5 µm (specimen designation: ROI-0 J-repair). To further characterize the specimen's micro-structure, a small cylinder of ~6.5 mm length was digitally extracted from the ROI image and then segmented, where segmentation is the partitioning of a gray-scale image into multiple disjoint regions, each of them homogeneous with respect to certain properties [50] using Mango, a software tool developed at the ANU specifically to work with tomographic data [50]. The small cylinder tomogram (gray-scale) and segmented (binary) volumetric data were then rendered in 3D using Drishti [51]. The resulting images were used to investigate and characterize the specimen's microstructure in detail. Micro-CT images' total acquisition time varied between 20 h (overview of the six samples), 39 h (ROI-0 J-repair) and 14 h (ROI-5 J/20 J-repair/virgin), which warranted for the acquisition of high quality (i.e. favorable signal-to-noise ratio) scans.

2. Results and discussion

2.1. Mechanical testing

Figure 2(a)–(d) shows the force vs. time history (mean curve) of the virgin in comparison to the repaired specimens as well as the standard deviation, which is indicated as shaded area. The standard deviation is most pronounced for the 30 J impact as depicted in Fig. 2(d). It can be noted that the maximum forces as well as the duration of the impact process increase with increasing impact energy from below 3000 N and ~5 ms in the case of the 5 J impact to ~4500 N and ~9 ms in the case of

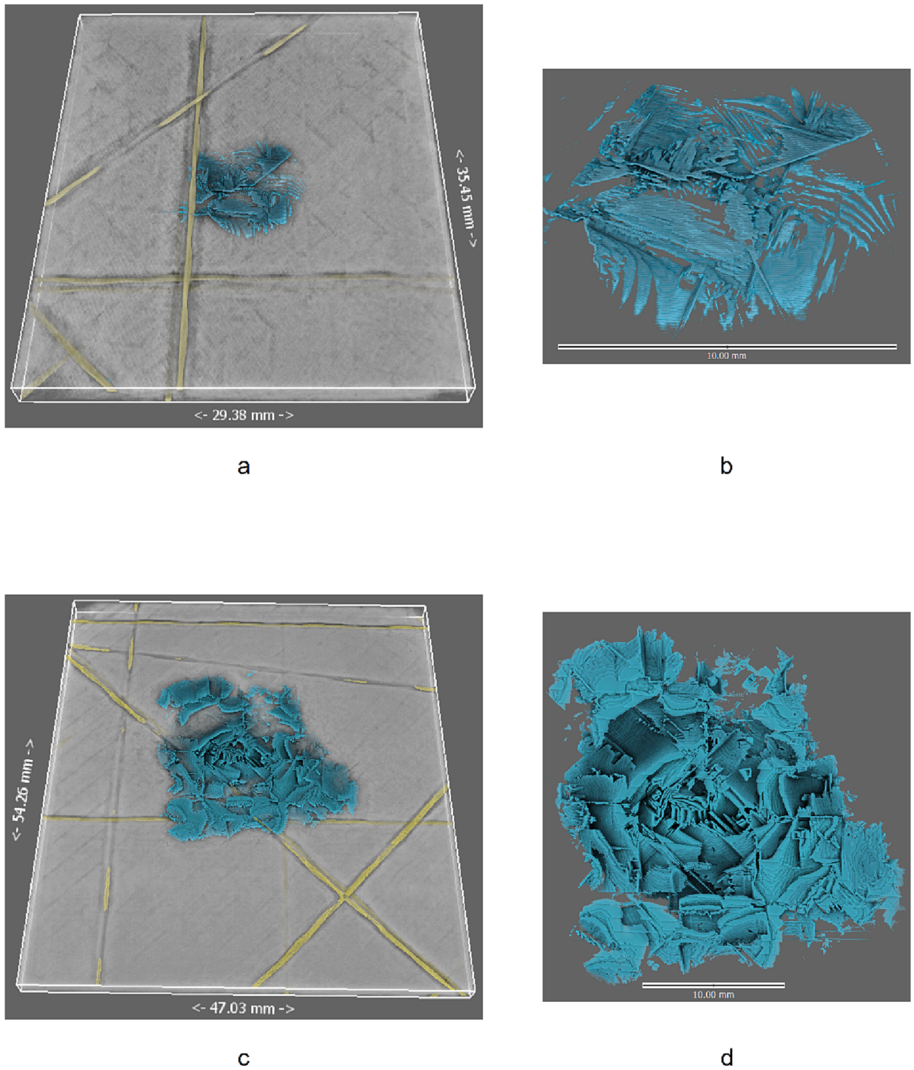

Fig. 7. 3D visualizations focusing on the damage volume of the virgin samples: (a) and (b) 5 J impact (ROI-5 J-virgin) as well as (c) and (d) 20 J impact (ROI-20 J- virgin).

the 30 J impact, respectively in the case of the virgin specimens. These trends are in accordance with literature for various combinations of fiber and matrix as well as specimen thickness: Kumari et al. (glass fiber reinforced vinyl ester cross-ply laminate, thickness of 4.8 mm) [37], Jefferon Andrew et al. (glass fiber reinforced, epoxy-based laminates, thickness of 2.0 mm) [52], Ivañez et al. (carbon fiber reinforced, epoxy based quasi-isotropic laminates, thickness of 2.0 mm) [23] as well as Jang and Kim (carbon fiber reinforced, epoxy based quasi-isotropic laminates, thickness of 5.1 mm) [53].

The general trends for the repaired specimens are comparable to the virgin specimens. However, contrary to the virgin specimens, for the repaired specimens impacted with 20 J, a significant increase in the maximum force occurred compared to the 10 J impacts. For the virgin specimens, the most significant increase was monitored between 20 J and 30 J. Compared to the virgin specimens, the repaired specimens show a higher peak force at the respective impact energy levels, which can be attributable to their increased thickness in the tapered region, leading to an increase in bending stiffness [23].

Regarding the influence of the impact events on the post-impact mechanical properties, stress vs. strain plots as a function of impact energy are depicted in Fig. 3. Again, the plot consists of mean curves and includes the standard deviation (shaded area) for the respective curves. A significant decrease in both, post impact strength as well as strain at break can be observed with increasing impact energy, which is in accordance with literature as well [37,52]. The tensile strength as well as the strain at break decreased with increasing impact energy from 550 ± 17 MPa/1.3 ± 0.03 % (non-impacted, i.e. 0 J) to 448 ± 14 MPa/1.1 ± 0.04 % (5 J impact), 361 ± 8 MPa/0.9 ± 0.02 % (10 J impact), 257 ± 8 MPa/0.7 ± 0.02 % (20 J impact) and 197 ± 11 MPa/0.6 ± 0.03 % (30 J impact) respectively.

With the impact energy exceeding 10 J, a deviation in the slope of the stress vs. strain plots becomes apparent. The decrease in stiffness for the 20 J and 30 J impacts could be related to the extent and type of damage resulting from the impact events [54]. In contrast, the specimens impacted with 5 J and 10 J show a similar slope as the undamaged (0 J) specimens.

The according post-impact mean stress vs. strain diagrams as a function of impact energy are plotted in Fig. 4 for the repaired specimens. Except for the 10 J impact, the repaired specimens' stress and strain response to the quasi-static tensile loading conditions was comparable to the virgin specimens' response. The tensile stress of the repaired specimens in undamaged state (non-impacted, i.e. 0 J) was found to be 542 ± 4 MPa, the strain at break 1.3 ± 0.02 %. For the impacted specimens, the respective material properties were found to be: 447 ± 9 MPa/1.0 ± 0.03 % (5 J impact), 262 ± 29 MPa/0.7 ± 0.05 % (10 J impact), 265 ± 22 MPa/0.7 ± 0.05 % (20 J impact) and 203 ±

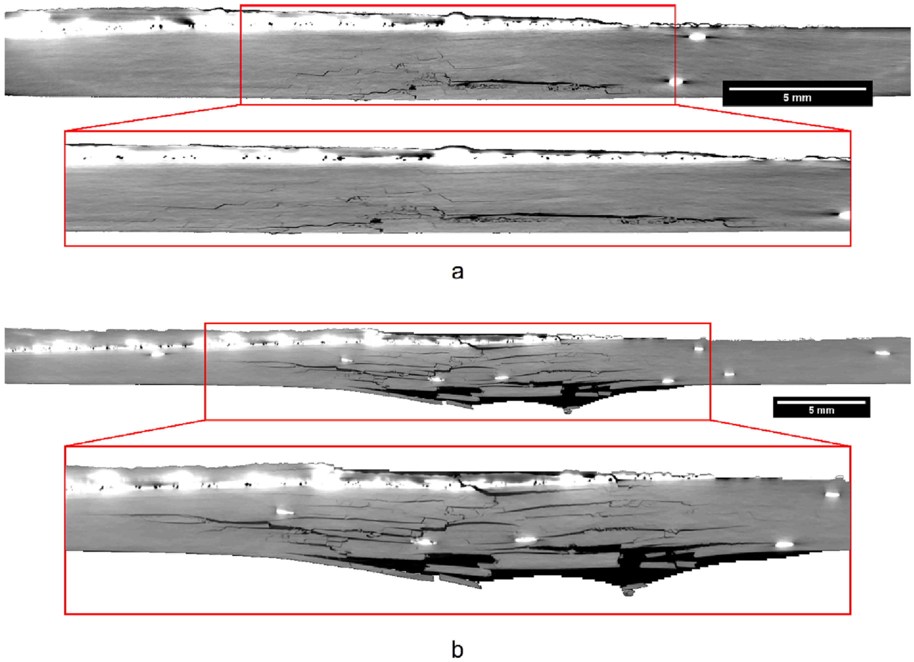

Fig. 8. 2D tomogram images of repaired samples impacted with (a) 5 J (ROI-5 J-repair, scanning resolution of 14 µm) and (b) 20 J (ROI-20 J-repair, scanning resolution of 19 µm). Please note that the scalebars have been inserted manually using ImageJ [57].

13 MPa/0.6 ± 0.04 % (30 J impact). As indicated, the 10 J impacted repair-specimens showed lower tensile strength as well as strain at break levels than the according virgin specimens (see Fig. 3 for comparison). Additionally, the decrease in stiffness occurred at a lower impact energy level of 10 J for the repair-specimens than for the virgin specimens. In the latter case, the decrease was found for the 20 J and 30 J impact events.

An interesting aspect is, that the repaired specimens, except for the 10 J impact, performed comparable to the virgin specimens in terms of maximum stress and strain. This is in contradiction of literature results from e.g. Kumari et al. [37]. However, Kumari et al. were working with glass fiber reinforced cross ply laminates impregnated with vinyl ester resin repaired with a hard patch repair approach, a different repair geometry, i.e. 3D repair, as well as with a different taper ratio [37]. In the present study, a taper ratio of 1:30 was used, leading to a taper angle of 1.9°, whereas in the study by Kumari et al., the taper angle was 10° [37].

2.2. Computed tomography

In micro-CT images, the X-ray attenuation value for any material scanned is a function of the energy of the instrument's X-ray source used to acquire the scan and of the material's density and atomic number [55,56]. In general, the lower a material's density is, the lower its attenuation to the beam becomes, hence the darker it will appear in the grayscale reconstructed image; at the same time, the higher a material's density is, the brighter it will appear in the image [55,56]. As a result, voids and/or fractures/cracks, if present, constituting of air, are usually the darkest phase in an image [55,56].

The image of the ROI-0 J-repair specimen depicted in Fig. 5(a) shows the individual components forming the repair-specimens, which are magnified in Fig. 5(b), (marked as "Detail 1" in Fig. 5(a)): (i) the carrier (low attenuating knit polyester) incorporated in (iii) the adhesive (high density material) as well as (ii) the tracer yarns (glass fibers) surrounded by the parent and repair laminate. Additionally, individual carbon fibers can be identified within the matrix material in both images, (a) and (b). In general, no voids or cracks could be found within the inspected volumes, implying that, if structural defects are present within the polymer structure, their size must be below the image spatial resolution, hence sub-micron. In addition, regions where the adhesive is mixed with the epoxy matrix were also recognized by an average beam attenuation value that is higher than the matrix and lower than pure adhesive.

3D visualizations of segmented images acquired from a subset of the ROI-0 J-repair image are depicted in Fig. 5(c)–(e). The tracer yarns could be segmented and are observable especially in Fig. 5(d). As observed from the previous images, the carrier possesses a very low attenuation value. In order to distinguish it from voids, that would be low attenuating as well, the segmentation of the adhesive and the carrier, respectively, was performed as well. The knitting pattern of the carrier is clearly visible in close detail in Fig. 5(e).

In Fig. 6, representative virtual cross-sectional 2D slices are presented. These images were acquired at a lower scanning resolution and show the virgin specimens impacted at 5 J and 20 J, designated (a)/(b), respectively. It can be seen that with the increase in impact energy from 5 J to 20 J, the extent of damage increases significantly. For the specimens impacted with 5 J, damage is visible on the face opposing the impact site and is extending towards the impact location. Several other 2D virtual cross-sectional images were digitally extracted parallel (X slices) and perpendicular (Y and Z slices) to the impact direction. From their visual inspection it is suggested that the damage propagates within the sample mainly as fractures through the matrix which appear to be a precursor to delamination. Some fiber fracture is also likely to take place; however, due to the relatively low resolution of the images, individual carbon fibers within the laminate cannot be distinguished from the surrounding matrix material. A similar analysis was conducted on cross-sectional images extracted from the 3D image of the specimen impacted with 20 J.

Beside punctuation damage, Fig. 6(b) shows a complex network of fractures propagating through the matrix which affect the full specimen thickness causing severe delamination and, most likely, extensive fiber fracture. Comparable observations were also made by Léonard et al. [18], who were working on micro-CT images of specimens consisting of carbon fibers impregnated with epoxy resin acquired at a voxel size of 35.7 µm.

For better visibility, information on the extent of damage in the entire specimen with respect to all 3 dimensions is presented in Fig. 7 as 3D-visualisations: (a) and (b) 5 J impact, (c) and (d) 20 J impact. From

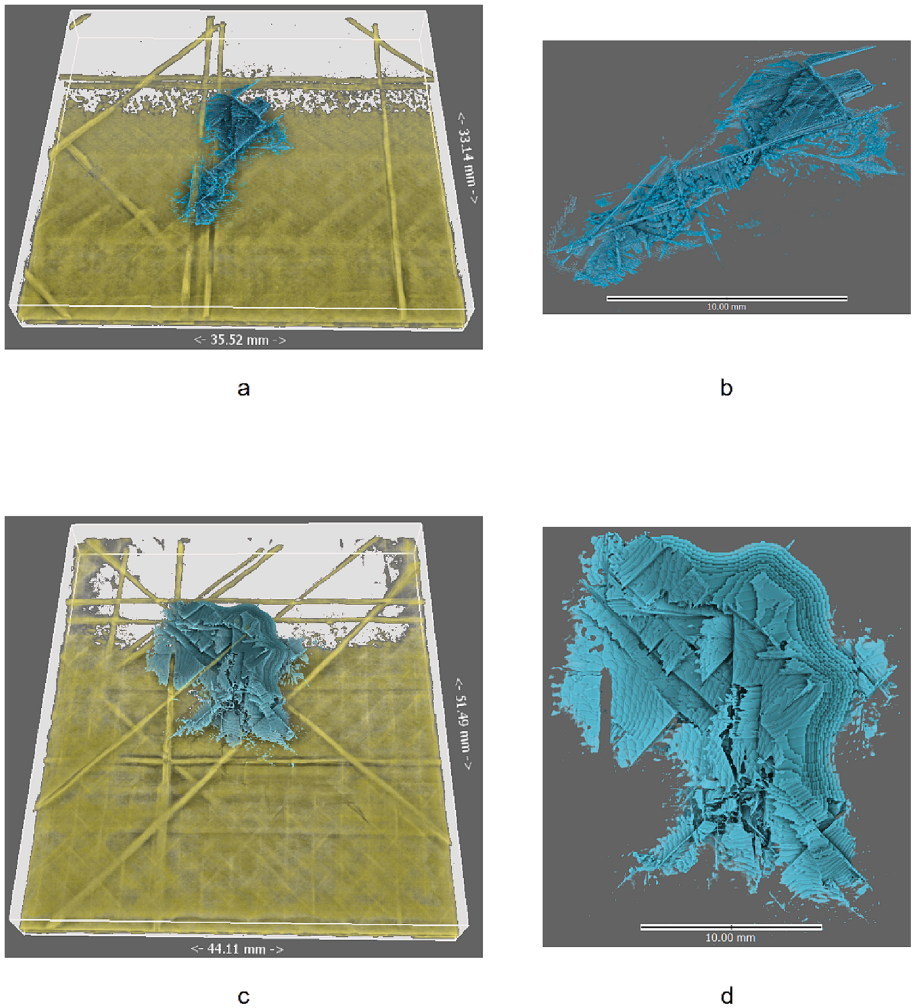

Fig. 9. 3D visualizations focusing on the damage volume of the repaired samples: (a) and (b) 5 J impact (ROI-5 J-repair) as well as (c) and (d) 20 J impact (ROI-20 J-repair).

these images it can be concluded that the damaged zone for both impact energies is significantly smaller compared to the width of the specimens used in the tensile tests (i.e. 80 mm).

Similar to the virgin specimens, several 2D virtual cross-sectional images were extracted from the 3D images acquired on the repaired samples impacted with 5 J and 20 J. One representative 2D image is shown in Fig. 8(a) and (b). A thorough inspection of the cross-sectional images suggests that failure mode, damage propagation and extent within the repaired specimens are overall very similar to what observed and previously described for the virgin samples, when impacted with the same energy.

In addition, while in the case of the 20 J impact (e.g. Fig. 8(b)), damage in the forms of matrix fractures, extensive delamination and fiber fracture (assumed) affect the whole specimen thickness by propagating through the adhesive and the adjacent parent- and repair-laminates, in the case of the 5 J impacted specimen (e.g. Fig. 8(a)), no sign of damage can be identified within the adhesive. Concluding from Fig. 9, where (a) and (b) correspond to the 5 J and (c) and (d) to 20 J impacts, the dimension of the damaged zone again does not extend across the full tensile specimen's width for both impact energies. For better comparison and depiction of the damage-extent and characterization of the damage-propagation throughout the entire specimen, **video 1** and **video 2** show comparative 3D visualizations of the repaired as well as the pristine specimens impacted with 20 J impact energy. In addition, **video 1**, also shows details of the adhesive and knit polyester.

A comparison of the projected in-plane damaged area depicted in Fig. 10 shows similarities between the virgin, i.e. 5 J (a) and 20 J impacted (b), as well as the repaired, i.e. 5 J (c) and 20 J impacted (d), specimens. However, it can be noted, that with respect to the in-plane damage area extension, a significant difference is visible between the 5 J and the 20 J impacts. The respective damaged areas (projected area) were found to be 115 mm^2 (virgin) and 147 mm^2 (repair) for the 5 J impacts as well as 687 mm^2 (virgin) and 718 mm^2 (repair) in the case of the 20 J impacts, respectively. For each imaged sample, the volumetric extension of the damage was then calculated by overlying the perimeter of the 2D damaged areas on top of the relevant 3D images, estimating the average thickness of the underlying portion of samples affected by some form of damage and multiplying 2D damaged areas by thickness. Estimated damaged volumes follow the damaged areas' trends, with a damaged volume of 290 mm^3 for the virgin and 440 mm^3 for the repaired specimens impacted with 5 J and a damaged volume of 1790 mm^3 for the virgin and 2250 mm^3 for the repaired specimens impacted with 20 J. It should be noted that for the samples impacted with 20 J, the volumetric extension of the damage is likely to be underestimated given that the damage propagates throughout the full thickness of the samples, in both virgin and repaired cases.

3. Conclusion

In the first section of the present study, impact as well as tension after impact tests were performed on repaired as well as pristine (virgin) specimens produced from quasi-isotropic laminates (woven carbon

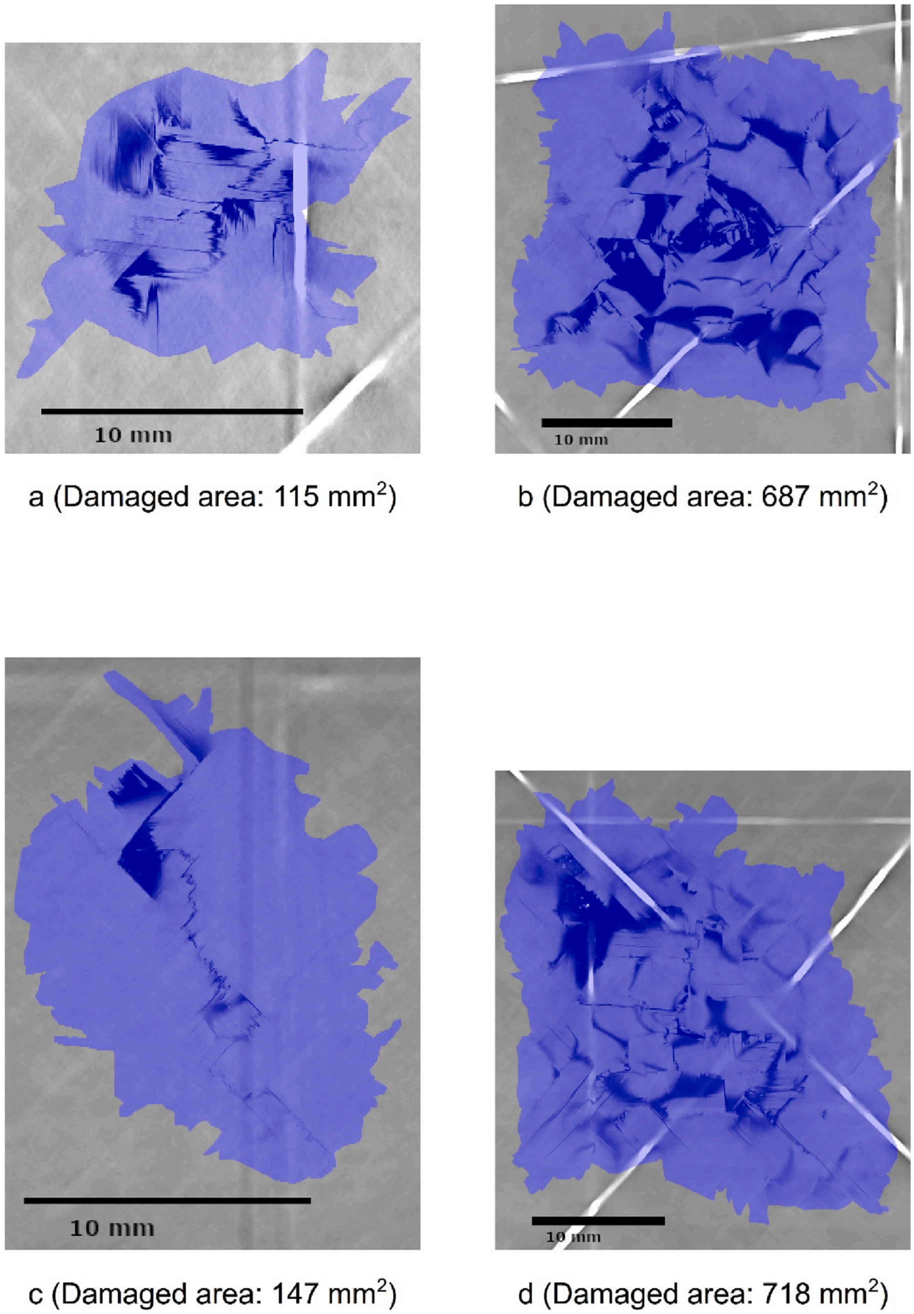

Fig. 10. 2D projections of the total damage area (including numerical value) for the impacted specimens: (a) ROI-5 J-virgin (b) ROI-20 J-virgin (c) ROI-5 J-repair (d) ROI-20 J-repair.

fibers impregnated with epoxy matrix resin, stacking sequence $[(\pm45)/(0/90)/(\pm45)/(0/90)]_S$). The repairs were conducted via a soft-patch repair approach restoring the original stacking sequence of the laminate.

The aim was to investigate the post-impact mechanical properties of the repaired specimens in comparison to the pristine laminate in dependency of the impact energy. For both, the pristine as well as the repaired specimens, the maximum impact force as well as the duration of the impact process increased with increasing impact energy. The quasi-static tensile tests showed a decrease in the mechanical properties, i.e. tensile strength, strain at break and stiffness, with increasing impact energy for the repaired as well as the pristine laminates.

The second section of the study was aimed at the detailed investigation of the non-impacted, repaired specimens as well as the post-impact damage on repaired as well as pristine laminates via CT inspection. It could be shown, that via micro-CT the individual constituents of the bonded repairs could be identified and segmented. This was especially important in the case of the low-attenuating carrier, which could be distinguished from voids by the identification of its knitting pattern in 3D representations. For the damaged laminates, the extent of damage could be visualized via 2D cross-sectional slices and 3D visualizations. The damaged area could be compared qualitatively and quantitatively for the pristine as well as the repaired specimens by the use of 2D projections as well as by assessment of the volumetric extensions. Similarities in the extent of damage were found between the pristine as well as the repaired specimens. It could furthermore be shown that in the case of the repaired specimens, damage extended into the adhesive layer. Furthermore, comparative videos showing in great detail the damage extent and propagation within the entire specimen were produced for the two 20 J energy impact samples.

Within this work, specimens were tested at room temperature only.

In further research, special emphasis has to be laid on the conditions relevant for aircraft repairs, e.g. increased test temperature or conditioning under hot/wet conditions or in fluids typically used within aircraft service or during maintenance.

Funding

The research work of this paper was performed at the Polymer Competence Center Leoben GmbH (PCCL, AT) within the framework of the COMET-program (854178) of Federal Ministry for Climate Action, Environment, Energy, Mobility, Innovation and Technology and the Federal Ministry for Digital and Economic Affairs with contributions by Montanuniversitaet Leoben (Chair of Material Science and Testing of Polymers, AT), the FACC Operations GmbH (AT). The PCCL is funded by the Austrian Government and the State Governments of Styria, Lower Austria and Upper Austria.

The ANU component of this project was conducted within the ARC Training Centre for Automated Manufacture of Advanced Composites (IC160100040), supported by the Commonwealth of Australia under the Australian Research Council's Industrial Transformation Research Program.

CRediT authorship contribution statement

Florian Roeper: Conceptualization, Methodology, Investigation, Writing – original draft, Visualization. **Silvano Sommacal:** Conceptualization, Methodology, Investigation, Writing – original draft, Visualization. **Paul Compston:** Conceptualization, Resources, Writing – review & editing, Supervision, Project administration, Funding acquisition. **Jürgen Tauchner:** Resources, Project administration. **Markus Wolfahrt:** Resources, Writing – review & editing, Supervision, Project administration, Funding acquisition. **Gerald Pinter:** Resources, Writing – review & editing.

Declaration of Competing Interest

The authors declare that they have no known competing financial interests or personal relationships that could have appeared to influence the work reported in this paper.

Data availability

The data that has been used is confidential.

Acknowledgements

The authors would like to thank Sebastian Maar, Stefan Oberfrank, Chris Stokes-Griffin, and Jürgen Grosser as well as Georg Kucher, Constantinos Bouras and Rene Adam for their support. For the technical support, the authors wish to thank the ANU's X-ray tomography team. We also thank the ANU Supercomputer Facility and National Computational Infrastructure (NCI) for their generous allocation of compute time.

Appendix A. Supplementary data

Supplementary data to this article can be found online at https://doi.org/10.1016/j.compstruct.2023.117338.

References

[1] Guermazi N, Ben Tarjem A, Ksouri I, Ayedi HF. On the durability of FRP composites for aircraft structures in hygrothermal conditioning. Compos B 2016;85:294–304. https://doi.org/10.1016/j.compositesb.2015.09.035.

[2] Alessi S, Pitarresi G, Spadaro G. Effect of hydrothermal ageing on the thermal and delamination fracture behaviour of CFRP composites. Compos B 2014;67:145–53. https://doi.org/10.1016/j.compositesb.2014.06.006.

[3] La Saponara V. Environmental and chemical degradation of carbon/epoxy and structural adhesive for aerospace applications: Fickian and anomalous diffusion, Arrhenius kinetics. Compos Struct 2011;93(9):2180–95. https://doi.org/10.1016/j.compstruct.2011.03.005.

[4] Wang CH, Venugopal V, Peng L. Stepped flush repairs for primary composite structures. J Adhes 2015;91(1–2):95–112. https://doi.org/10.1080/00218464.2014.896212.

[5] Yoo J-S, Truong V-H, Park M-Y, Choi J-H, Kweon J-H. Parametric study on static and fatigue strength recovery of scarf-patch-repaired composite laminates. Compos Struct 2016;140:417–32. https://doi.org/10.1016/j.compstruct.2015.12.041.

[6] Harder S, Grossheider K, Hergoss P, Schmutzler H, Fiedler B. Ytterbium fibre laser surface pre-treatment of CFRP soft patch repairs. In: Society for the Advancement of Material and Process Engineering, editor. SAMPE Conference 2017 Stuttgart Proceedings; 2017. p. 1–8.

[7] Katnam KB, Da Silva L, Young TM. Bonded repair of composite aircraft structures: A review of scientific challenges and opportunities. Prog Aerosp Sci 2013;61:26–42. https://doi.org/10.1016/j.paerosci.2013.03.003.

[8] Baker AA. A proposed approach for certification of bonded composite repairs to flight-critical airframe structure. Appl Compos Mater 2011;18(4):337–69. https://doi.org/10.1007/s10443-010-9161-z.

[9] Ahn S-H, Springer GS. Repair of Composite Laminates. Stanford: CA, US; 2000.

[10] Kumar SB, Sridhar I, Sivashanker S, Osiyemi SO, Bag A. Tensile failure of adhesively bonded CFRP composite scarf joints. Mater Sci Eng B 2006;132(1–2):113–20. https://doi.org/10.1016/j.mseb.2006.02.046.

[11] Salah L. Weak interfacial bonds and the long-term durability of bonded repairs to polymer matrix composites [Dissertation]. Wichita: Wichita State University; 2012.

[12] Hayes-Griss JM, Gunnion AJ, Afaghi KA. Damage tolerance investigation of high-performance scarf joints with bondline flaws under various environmental, geometrical and support conditions. Compos A 2016;84:246–55. https://doi.org/10.1016/j.compositesa.2016.02.005.

[13] Schmutzler H, Popp J, Büchter E, Wittich H, Schulte K, Fiedler B. Improvement of bonding strength of scarf-bonded carbon fibre/epoxy laminates by Nd:YAG laser surface activation. Compos A 2014;67:123–30. https://doi.org/10.1016/j.compositesa.2014.08.029.

[14] Harder S, Schmutzler H, Hergoss P, Freese J, Holtmannspötter J, Fiedler B. Effect of infrared laser surface treatment on the morphology and adhesive properties of scarfed CFRP surfaces. Compos A 2019;121:299–307. https://doi.org/10.1016/j.compositesa.2019.02.025.

[15] Röper F, Wolfahrt M, Schlögl S, Kucher G, Pinter G. Bonded aerospace repairs under tensile loading: Wet chemical surface treatment and selected environmental conditions. J Appl Polym Sci 2019;42:47506. https://doi.org/10.1002/app.47506 (1-9).

[16] Shufeng L, Xiaoquan C, Yunyan X, Jianwen B, Xin G. Study on impact performances of scarf-repaired carbon fiber reinforced polymer laminates. J Reinf Plast Compos 2015;34(1):60–71. https://doi.org/10.1177/0731684414562465.

[17] Slattery PG, McCarthy CT, O'Higgins RM. Assessment of residual strength of repaired solid laminate composite materials through mechanical testing. Compos Struct 2016;147:122–30. https://doi.org/10.1016/j.compstruct.2016.03.036.

[18] Léonard F, Stein J, Soutis C, Withers PJ. The quantification of impact damage distribution in composite laminates by analysis of X-ray computed tomograms. Compos Sci Technol 2017;152:139–48. https://doi.org/10.1016/j.compscitech.2017.08.034.

[19] Kim C-H, Sim H-W, An W-J, Kweon J-H, Choi J-H. Impact characteristics of composite panel stitched by I-fiber process. Compos Part A 2019;127. https://doi.org/10.1016/j.compositesa.2019.105644 (1-8).

[20] Park H, Kong C. A study on low velocity impact damage evaluation and repair technique of small aircraft composite structure. Compos A 2011;42(9):1179–88. https://doi.org/10.1016/j.compositesa.2011.05.002.

[21] Jefferson Andrew J, Arumugam V, Saravanakumar K, Dhakal HN, Santulli C. Compression after impact strength of repaired GFRP composite laminates under repeated impact loading. Compos Struct 2015;133:911–20. https://doi.org/10.1016/j.compstruct.2015.08.022.

[22] Ivañez I, Garcia-Castillo SK, Sanchez-Saez S, Barbero E. Experimental study of the impact behavior of repaired thin laminates with double composite patch. Mech Adv Mater Struct 2020;27(19):1701–8. https://doi.org/10.1080/15376494.2018.1524952.

[23] Ivañez I, Garcia-Castillo SK, Sanchez-Saez S, Barbero E. Analysis of the impact location on damage tolerance of bonded-repaired composite laminates. Polymer Testing 2019;78. https://doi.org/10.1016/j.polymertesting.2019.106000 (1-10).

[24] Xia G, Zengshan L, Hengchang N, Wei H, Zhidong G. Impact resistance and damage tolerance of scarf-repaired composite structures: An experimental investigation. Polym Compos 2016;37(6):1681–94. https://doi.org/10.1002/pc.23341.

[25] Hogg PJ, Bibo GA. Impact and damage tolerance. In: Hodgkinson JM, editor. Mechanical testing of advanced fibre composites. Boca Raton, FL, Cambridge, England: CRC Press; 2000. p. 211–47.

[26] Malhotra A, Guild FJ. Impact Damage to Composite Laminates: Effect of Impact Location. Appl Compos Mater 2014;21(1):165–77. https://doi.org/10.1007/s10443-013-9382-z.

[27] Riccio A, Saputo S, Sellitto A, Russo A, Acanfora V, Iaccarino P, et al. On the mechanical behavior of laminated composite plates subjected to compression after impact tests. Mater Today: Proc 2021;34:53–6. https://doi.org/10.1016/j.matpr.2020.01.184.

[28] Anuse VS, Shankar K, Velmurugan R, Ha SK. Compression-After-Impact analysis of carbon fiber reinforced composite laminate with different ply orientation sequences. Int J Impact Eng 2022;167:104277. https://doi.org/10.1016/j.ijimpeng.2022.104277.

[29] Lin S, Ranatunga V, Waas AM. Experimental study on the panel size effects of the low velocity impact (LVI) and compression after impact (CAI) of laminated composites, part II: CAI. Compos Struct 2022;295:115824. https://doi.org/10.1016/j.compstruct.2022.115824.
[30] Yang B, Chen Y, Lee J, Fu K, Li Y. In-plane compression response of woven CFRP composite after low-velocity impact: Modelling and experiment. Thin-Walled Struct 2021;158:107186. https://doi.org/10.1016/j.tws.2020.107186.
[31] Biagini D, Pascoe J-A, Alderliesten R. Investigation of compression after impact failure in carbon fiber reinforced polymers using acoustic emission. J Compos Mater 2023;57(10):1819–32. https://doi.org/10.1177/00219983231163853.
[32] Sanchez-Saez S, Barbero E, Zaera R, Navarro C. Compression after impact of thin composite laminates. Compos Sci Technol 2005;65(13):1911–9. https://doi.org/10.1016/j.compscitech.2005.04.009.
[33] Remacha M, Sánchez-Sáez S, López-Romano B, Barbero E. A new device for determining the compression after impact strength in thin laminates. Compos Struct 2015;127:99–107. https://doi.org/10.1016/j.compstruct.2015.02.079.
[34] Kim M. Impact resistance of composite scarf joints under load. Melbourne, AU: RMIT University; 2010.
[35] Cheng X, Zhao W, Liu S, Xu Y, Bao J. Damage of scarf-repaired composite laminates subjected to low-velocity impacts. Steel Compos Struct 2014;17(2):199–213. https://doi.org/10.12989/scs.2014.17.2.199.
[36] Harman AB, Rider AN. Impact damage tolerance of composite repairs to highly-loaded, high temperature composite structures. Compos A 2011;42(10):1321–34. https://doi.org/10.1016/j.compositesa.2011.05.015.
[37] Kumari P, Wang J, Saahil. Tensile after impact test of scarf-repaired composite laminates. Arab J Sci Eng 2019;44(9):7677–97. https://doi.org/10.1007/s13369-019-03857-z.
[38] Feng W, Xu F, Xie W, Wang A, Ma C. Impact and tension-after-impact behaviors of scarf-repaired composite laminates: An experimental and numerical approach. Mech Adv Mater Struct 2023;30(6):1260–73. https://doi.org/10.1080/15376494.2022.2029983.
[39] Bull DJ, Helfen L, Sinclair I, Spearing SM, Baumbach T. A comparison of multi-scale 3D X-ray tomographic inspection techniques for assessing carbon fibre composite impact damage. Compos Sci Technol 2013;75:55–61. https://doi.org/10.1016/j.compscitech.2012.12.006.
[40] Bull DJ, Spearing SM, Sinclair I. Observations of damage development from compression-after-impact experiments using ex situ micro-focus computed tomography. Compos Sci Technol 2014;97:106–14. https://doi.org/10.1016/j.compscitech.2014.04.008.
[41] Senck S, Scheerer M, Revol V, Plank B, Hannesschläger C, Gusenbauer C, et al. Microcrack characterization in loaded CFRP laminates using quantitative two- and three-dimensional X-ray dark-field imaging. Compos A 2018;115:206–14. https://doi.org/10.1016/j.compositesa.2018.09.023.
[42] ASTM International - D30 Committee, Test Method for Measuring the Damage Resistance of a Fiber-Reinforced Polymer Matrix Composite to a Drop-Weight Impact Event (ASTM D7136 / D7136M - 15). West Conshohocken, PA: ASTM International; 2015, doi: 10.1520/D7136_D7136M-15; Available from: https://www.astm.org/Standards/D7136.htm. [September 10, 2019].
[43] DIN Deutsches Institut für Normung e. V. Determination of tensile strength of tapered and stepped joints. 1st ed., 49.040.10. Berlin, DE: Beuth Verlag GmbH; 1995. [April 01, 2016].
[44] Cytec Engineered Materials. Cycom®977-2 Epoxy resin system: Technical data sheet; AECM-00007; REV: 01; 19 March 2012. [April 24, 2018]; Available from: http://www.cytec.com/sites/default/files/datasheets/CYCOM_977-2_031912.pdf.
[45] 3M Company, 3M Scotch-Weld™ Structural Adhesive Film AF 163-2: Technical Datasheet November 2009. [April 24, 2018]; Available from: https://multimedia.3m.com/mws/media/282041O/3m-scotch-weld-structural-adhesive-film-af-163-2-af-163-3.pdf.
[46] Dorworth LC, Gardiner GL, Mellema GM. Essentials of advanced composite fabrication and repair. Newcastle, Wash: Aviation Supplies & Academic; 2009.
[47] Wang CH, Duong CN. Bonded joints and repairs to composite airframe structures. London: Academic Press is an imprint of Elsevier; 2016.
[48] Cytec Industries Inc. FM® 300 Epoxy Film Adhesive: Technical data sheet; AEAD-00002; Rev. 02; 9 October 2013. [April 24, 2018]; Available from: http://www.cytec.com/sites/default/files/datasheets/FM_300_081211-08a.pdf.
[49] Sheppard A, Latham S, Middleton J, Kingston A, Myers G, Varslot T, et al. Techniques in helical scanning, dynamic imaging and image segmentation for improved quantitative analysis with X-ray micro-CT. Nucl Instrum Methods Phys Res, Sect B 2014;324:49–56. https://doi.org/10.1016/j.nimb.2013.08.072.
[50] Sheppard AP, Sok RM, Averdunk H. Techniques for image enhancement and segmentation of tomographic images of porous materials. Phys A 2004;339(1–2):145–51. https://doi.org/10.1016/j.physa.2004.03.057.
[51] Limaye A. Drishti: a volume exploration and presentation tool. In: Stock SR, editor. Developments in X-Ray Tomography VIII. SPIE; 2012, 85060X-1-9.
[52] Jefferson Andrew J, Srinivasan SM, Arockiarajan A. The role of adhesively bonded super hybrid external patches on the impact and post-impact response of repaired glass/epoxy composite laminates. Compos Struct 2018;184:848–59. https://doi.org/10.1016/j.compstruct.2017.10.070.
[53] Jang B-W, Kim C-G. Real-time detection of low-velocity impact-induced delamination onset in composite laminates for efficient management of structural health. Compos B 2017;123:124–35. https://doi.org/10.1016/j.compositesb.2017.05.019.
[54] Tan W, Falzon BG, Chiu LN, Price M. Predicting low velocity impact damage and Compression-After-Impact (CAI) behaviour of composite laminates. Compos A 2015;71:212–26. https://doi.org/10.1016/j.compositesa.2015.01.025.
[55] Stock SR. X-ray microtomography of materials. Int Mater Rev 1999;44(4):141–64. https://doi.org/10.1179/095066099101528261.
[56] Michael G. X-ray computed tomography. Phys Educ 2001;36(6):442–51. https://doi.org/10.1088/0031-9120/36/6/301.
[57] Rasband W.S. ImageJ . Bethesda, Maryland, USA: National Institutes of Health; 1997-2015.